Check for updates

JGR Atmospheres

RESEARCH ARTICLE
10.1029/2018JD029667

Key Points:
- Low clouds over ENA account for a significant (45%) contribution to the total rainfall
- Low cloud diurnal cycle suggests a rainfall peak during the overnight hours and a secondary peak after local noon
- Synoptic state (sfc pressure and 850-mb winds) exerts a significant control on low cloud properties including rainfall rate and drop size

Correspondence to:
S. E. Giangrande,
sgrande@bnl.gov

Citation:
Giangrande, S. E., Wang, D., Bartholomew, M. J., Jensen, M. P., Mechem, D. B., Hardin, J. C., & Wood, R. (2019). Midlatitude oceanic cloud and precipitation properties as sampled by the ARM Eastern North Atlantic Observatory. *Journal of Geophysical Research: Atmospheres*, *124*, 4741–4760. https://doi.org/10.1029/2018JD029667

Received 14 SEP 2018
Accepted 21 MAR 2019
Accepted article online 29 MAR 2019
Published online 26 APR 2019

©2019. American Geophysical Union. All Rights Reserved.

Midlatitude Oceanic Cloud and Precipitation Properties as Sampled by the ARM Eastern North Atlantic Observatory

Scott E. Giangrande[1], Die Wang[1], Mary Jane Bartholomew[1], Michael P. Jensen[1], David B. Mechem[2], Joseph C. Hardin[3], and Robert Wood[4]

[1]Environmental and Climate Sciences Department, Brookhaven National Laboratory, Upton, NY, USA, [2]Department of Geography and Atmospheric Science, University of Kansas, Lawrence, KS, USA, [3]Pacific Northwest National Laboratory, Richland, WA, USA, [4]Department of Atmospheric Sciences, University of Washington, Seattle, WA, USA

Abstract Marine low clouds are critical to the climate system because of their extensive coverage and associated controls on boundary layer dynamics and radiative energy balance. The primary foci for this study are marine low cloud observations over a heavily instrumented site on the Azores archipelago in the Eastern North Atlantic and their associated raindrop size distribution (DSD) properties, relative low cloud contributions to the precipitation, and additional sampling (instrument, environmental) considerations. The contribution from low clouds (e.g., cloud top < 4 km) to the overall precipitation over midlatitude oceans is poorly understood, in part because of the lack of coupled, high-quality measurements of precipitation and low cloud properties. Cloud regime and precipitation breakdowns performed for a multiyear (2014–2017) record emphasize diurnal precipitation and raindrop size distribution characteristics for both low and deeper clouds, as well as differences between the two disdrometer types used. Results demonstrate that marine low clouds over this Eastern North Atlantic location account for a significant (45%) contribution to the total rainfall and exhibit a diurnal cycle in cloud (thickness, top, and base) and precipitation characteristics similar to satellite records. Additional controls on observed surface rainfall characteristics of low clouds allowed by the extended ground-based facility data sets are also explored. From those analyses, it is suggested that the synoptic state exerts a significant control on low cloud and surface precipitation properties.

1. Introduction

The treatment of cloud and precipitation processes in global climate models represents a major source of uncertainty in model predictions for the potential impacts of climate change (e.g., IPCC, 2013). Boundary layer cloud (stratocumulus and trade cumulus) processes and properties are critical to the climate system because of their extensive coverage and their associated controls on boundary layer dynamics and radiative energy balance (e.g., Bony & Dufresne, 2005; Hartmann et al., 1992; Klein & Hartmann, 1993). The presence of boundary layer clouds is, on average, controlled by large-scale subsidence and the strength of a low-level temperature inversion (e.g., Klein, 1997; Klein & Hartmann, 1993; Slingo, 1987). Precipitation from boundary layer clouds strongly complicates their dynamics and has been found to be associated with mesoscale cloud organization, coalescence processing and scavenging of aerosols, evaporative cooling/cold pool circulations, and transitions of closed-cellular to open-cellular convection (e.g., Feingold et al., 1996; Rapp, 2016; Stevens et al., 2005; Wood et al., 2018; Zhou et al., 2017).

The Eastern North Atlantic (ENA) is a location with frequent marine boundary layer (MBL) and low cloud coverage but also encounters deeper clouds associated with midlatitude disturbances (e.g., Albrecht, Bretherton, et al., 1995; Albrecht, Jensen, et al., 1995; Rémillard et al., 2012; Wood et al., 2015). Previous studies indicate that the Azores region of the ENA experiences different cloud regimes with a frequency that is broadly similar to those experienced globally (e.g., Rémillard & Tselioudis, 2015; Tselioudis et al., 2013; Wood et al., 2015). This makes extended observations of cloud or precipitation at the Azores useful for evaluating large-scale models over a wide variety of cloudiness regimes. Moreover, the Azores is a unique site in the context of previous precipitation studies as it experiences both subtropical and midlatitude synoptic environments (e.g., Mechem et al., 2018; Rémillard & Tselioudis, 2015). The generalizability of ENA cloud and precipitation properties also suggests this location as an important anchor for refining remote sensing

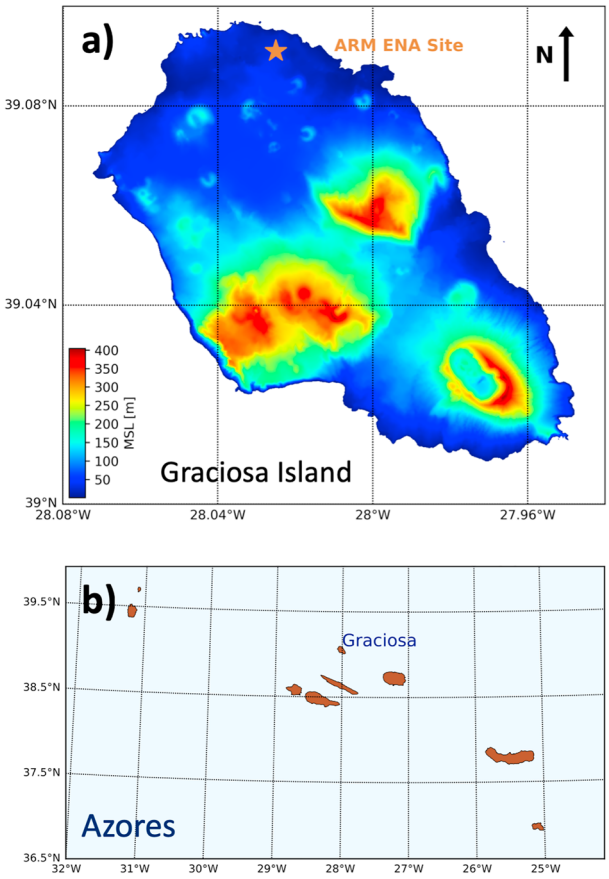

Figure 1. (a) Map of Graciosa Island showing terrain height (colors) and the location of the ARM ENA site. (b) Map of the location of Graciosa relative to the Azores archipelago. ARM = Atmospheric Radiation Measurement; ENA = Eastern North Atlantic; MSL = mean sea level.

capabilities, including profiling activities from spaceborne platforms (e.g., Hou et al., 2014; Stephens et al., 2002).

In 2013, the U.S. Department of Energy Atmospheric Radiation Measurement (ARM) Climate Research Facility established a permanent ENA site on Graciosa Island in the Azores, Portugal (e.g., Mather & Voyles, 2013). This site hosts several instruments for continuous cloud sampling, including vertically pointing millimeter wavelength radars collocated with multiple surface precipitation gauge and disdrometer units. This data set adds to the growing global precipitation archive, sampling oceanic precipitation from both deep and shallow clouds not well captured by previous deployments (e.g., Dolan et al., 2018). Azores observations also complement the oceanic cloud information primarily available from satellite sensors (e.g., Elsaesser et al., 2010).

The primary foci for this study are marine low clouds and (i) their associated raindrop size distribution (DSD) properties, (ii) the relative low cloud contributions to the precipitation over Graciosa Island, and (iii) additional sampling (instrument and environmental) considerations. Breakdown of precipitation characteristics by cloud type (low and deep) emphasizes the diurnal precipitation cycle, DSD characteristics, and instrument comparisons therein. The representativeness of DSD observations at ENA is contrasted with those reported in previous studies. This emphasis on rainfall is distinct from previous ENA precipitation studies that primarily focus on drizzling clouds. For example, Rémillard et al. (2012) report that for a 35-event data set, Azores marine stratocumulus clouds generated precipitation 70% of the time, while "intense" drizzle rates (based on a near-surface radar reflectivity threshold of 0 dBZ) are rare and preferentially occur near sunrise/sunset (<5% of the cases). Yang et al. (2018) found drizzle in >80% of cloud radar profiles of marine stratocumulus observed over a 20-month deployment of the ARM mobile facility (Miller et al., 2016) on Graciosa Island (Wood et al., 2015), with precipitation reaching the surface in 30% of the profiles. Measurable surface precipitation therefore occurs in a relatively small fraction of the total lower cloud coverage over the ENA site. However, this study demonstrates that low clouds account for a significant (45%) contribution to the total rainfall at the ENA site, with measurable precipitation reaching the surface on approximately half of the days during the multiyear study. Furthermore, we will discuss both microphysical (collisional growth and evaporation) and environmental controls on observed surface rainfall characteristics of shallow clouds. Cloud properties and precipitation processes broken down according to 850-mb horizontal winds and surface pressure will be used to argue the importance of synoptic variability.

2. The ARM ENA Site: Instruments and Data Set Processing Overview

The observations for this study were collected at the Graciosa Island ARM ENA facility (herein, we disambiguate ENA as the ARM Graciosa facility) in the Azores, Portugal archipelago (Figure 1). The data set is a multiyear record of collocated surface observations (2014–2017). The ARM facility is situated near the northern coast of the island. Clouds advecting from westerly and northerly flows are often assumed to be arriving from the open ocean and therefore are less influenced by island orography (Houze, 2012).

2.1. The KAZR

The radar for this study is the Ka-band ARM Zenith Radar (KAZR) vertically pointing 35 GHz (8-mm wavelength, 0.3° beam width) Doppler radar (e.g., Kollias et al., 2014). This radar has previously demonstrated reasonable sensitivity (−45 dBZ at 1 km) for MBL cloud studies in nonprecipitating and drizzling cloud conditions (e.g., Yang et al., 2018). The function of this radar in this study is to classify cloud regime (e.g., Low and Deep) and cloud properties associated with surface precipitation measurements (as similar to Rémillard et al., 2012). Cloud properties (base and thickness) are determined using the ARM multisensor Active

Remote Sensing of CLouds (ARSCL; Atmospheric Radiation Measurement (ARM) Climate Research Facility, 1996; Clothiaux et al., 2000) product. ARSCL products merge observations from the KAZR and a collocated laser ceilometer and microwave radiometer to better identify cloud properties at high temporal (~10-s) and vertical (~24-m) resolution. The properties are averaged to a 5-min record temporally aligned with surface disdrometer measurements. KAZR measurements experience partial attenuation in cloudy conditions; however, relative cloud properties, classifications and/or cloud thickness estimates (especially. in light rain) should not be biased significantly by KAZR sampling limitations (e.g., Giangrande et al., 2016). For example, ARSCL cloud base is designated by using a ceilometer that is unaffected by attenuation in rain/drizzle.

2.2. The ARM Parsivel^2 and 2DVD

Surface precipitation is measured by two primary instruments, a second-generation Parsivel disdrometer (hereafter, PARS, e.g., Bartholomew, 2014; Löffler-Mang & Joss, 2000; Tokay et al., 2014) and a two-dimensional video disdrometer (hereafter, 2DVD, e.g., Kruger & Krajewski, 2002). The collocated sensors capture the surface DSD from which we estimate DSD parameters and radar quantities of interest. These quantities include rainfall rate R (mm/hr), liquid water content LWC (g/m^3), median volume drop diameter $D0$ (mm), and additional calculations for normalized DSD parameters including the intercept Nw (e.g., Bringi et al., 2002, 2003, 2009; Testud et al., 2001). These measurements are most appropriate for moderate to larger raindrop sampling (e.g., drops >1 mm) and are not expected to sample drizzle or very small drops given disdrometer resolution >200 μm.

Disdrometer processing was performed using the open-source PyDSD code (Hardin, 2014), with standard corrections (e.g., Tokay et al., 2013, 2014) that includes drop removal based on fall speed and size (to remove drops as from splashing or other artifacts). This processing removes the smallest disdrometer size bin (e.g., Tokay et al., 2013) and any drops larger than 5 mm as unreliable. Disdrometer quantities are estimated using an assumption for the raindrop fall speed relationship following Lhermitte (2002). Radar quantities of interest including radar reflectivity factor Z are estimated for the X-band (3-cm) and Ka-band (8-mm) radar wavelengths at 20 °C using the T-matrix method as in PyDSD (e.g., Leinonen, 2014; Mishchenko, 2000). These wavelengths are those most relevant for the ARM ENA facility radars. Additional details on disdrometer processing from previous ARM deployments and similar units are described in Giangrande, Bartholomew, et al. (2014), Giangrande, Collis, et al. (2014), Thompson et al. (2015), and Wang et al. (2018). For this data set, 5-min DSD aggregation windows are used to reduce possible noisiness found in 1-min light rain observations. Note, all DSD quantities are estimated using the native bin spacing of the disdrometer units. Comparisons performed using similar spacing for both instruments did not significantly impact the results presented by this study.

The data quality is also controlled by selecting DSDs that have a total number of drops >100. While applying thresholds of this sort are standard practice for disdrometer studies (noting the effective sampling area of the 2DVD is approximately double that of the PARS), these choices further limit our sampling within light rain conditions (e.g., the study typically considers $R > 0.1$ mm/hr). Using the 100-drop threshold, approximately 27% of the PARS rainfall accumulation over the 3 years (data set total, 48% of the sampled DSDs) was removed, as compared to 0.9% of the accumulation sampled by the 2DVD (53% of the sampled DSDs). Overall, total rainfall accumulation sampled from the 2DVD was less influenced by the choice of drop count threshold (approximately 5% difference in rainfall accumulation between the choice of a 100- and 500-drop threshold, as compared to 12% for the PARS). Collocated rain gauges available during portions of the ENA record indicate that disdrometer accumulations typically agreed to within 10% for total rainfall accumulation (not shown).

2.3. Additional ARM ENA Site Capabilities

The ENA site hosts a surface meteorology station and radiosonde launches every 6 hr. The closest available radiosonde to the DSD observations provides the thermodynamic profiling for this study. The most frequent 850-mb winds associated with measurable rainfall (interpolated to the 5-min DSD observations) are westerly (Figure 2), with modest variability that includes flows from the southeast to northeast. Following Rémillard and Tselioudis (2015), the most detrimental island influences on cloud properties over the ARM site are

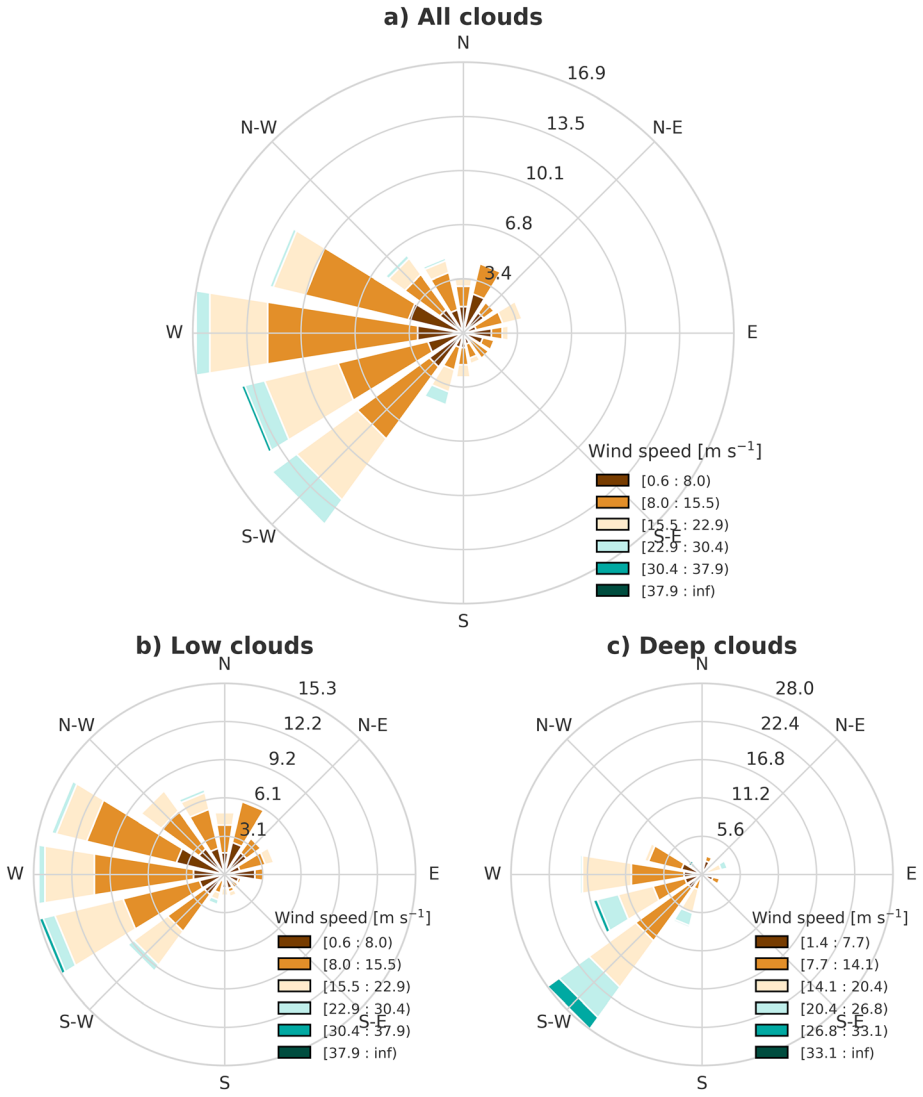

Figure 2. Wind roses (850 mb) for Eastern North Atlantic data set rainy events (a), Low cloud events (b), and Deep clouds events (c).

associated with a prominent southeasterly wind component. Those situations are associated with the Graciosa northeast-southwest island orientation and larger terrain features (e.g., Figure 1b).

3. The ENA Data Set: Overview of Cloud Regime Classification and Precipitation Attribution

The ENA record contains 14,722 DSDs meeting the processing criteria outlined in the previous section. These DSDs were associated with a total precipitation in excess of 1,200 mm, with an approximate 10% difference between the disdrometer types (accounting for the same threshold selection and KAZR availability) for a 3-year period (November 2014 to end of 2017). We distinguish the rainfall properties (DSD and accumulations) of lower clouds having radar-based echo top heights (ETHs) sampled below 4 km (hereafter "Low"), and from deeper cloud conditions commonly associated with frontal passages (hereafter "Deep"). This height-based definition is also associated with a relative minimum in the distribution of ETH for this data set (not shown).

The cloud regime classification adopted by this study is a conservative approach, as we do not claim to distinguish marine stratocumulus from other low or MBL cloud types such as shallow cumulus. The Low cloud category includes the canonical well-mixed stratocumulus-topped boundary layers but also clouds

associated with more complicated boundary layer structures such as multiple mixed layers and those in cold air outbreaks. This ETH definition is less restrictive than definitions adopted by Rémillard et al. (2012), who attempted to differentiate MBL clouds based on an additional criterion for cloud duration and/or ETH variability. From sensitivity testing, this choice (e.g., varying ETH from 2 to 4 km) influences our DSD interpretations in a predictable manner; for example, there is a minor reduction in the observed median drop sizes for clouds having lower ETH. Rainfall accumulations and additional discussions are reported as a function of ETH to demonstrate the cumulative impact of ETH designations throughout this study.

Overall, this data set contains 612 individual days with measurable surface rainfall (having a single 5-min DSD that can be classified as Low or Deep), with 199 of those days recording rainfall associated with a Deep cloud classification. For this data set, approximately 55% of the eligible days over ENA (wherein all instruments were functioning) were precipitation days, with 18% of the eligible days reporting a Deep cloud DSD. Low cloud precipitation and corresponding DSDs are associated with a wider range of 850-mb winds (Figure 2b), contingent on the location and strength of the Azores high and Icelandic low features in the Atlantic Ocean. Graciosa is situated toward the southern side of the winter-season midlatitude synoptic cyclone tracks (Wood et al., 2015). This generally promotes southwesterly flow over Graciosa predominantly associated with the warm sector region of the synoptic waves, particularly the area just ahead (south and east) of the cold front. The Deep cloud precipitation wind rose patterns (Figure 2c) are similar to those found in Rémillard and Tselioudis (2015), with their "frontal" conditions also favoring a southwesterly component.

4. Seasonal and Cloud Regime Precipitation Breakdowns: An Intercomparison of ENA Disdrometer Performance and Relationships With Previous Studies

4.1. Annual and Diurnal Breakdowns for the ENA Disdrometer Data Set

Monthly accumulation breakdowns for the data set (stacked histograms, Figure 3a) shows potential sampling limitations when considering a 3-year period (or any shorter-term record) as a representative ENA annual cycle. Several months show enhanced values of precipitation, which we speculate is associated with a small number of strong synoptic cyclone passages (e.g., Deep events have been isolated, as in Figure 3c). For example, the accumulations observed during May within this record are outliers to a simple single harmonic cycle. Over a shorter record, this variability is reasonable for ENA noting an enhanced peak storm occurrence for May over the northeast and northwest quadrants of the Azores as reported by Rémillard & Tselioudis (2015, their Figure 5). Moreover, this variability is expected when considering the 33-year record summarized by Rémillard and Tselioudis (2015), as months excluding the summertime (June–August, JJA) experience the passage of midlatitude storm conditions an average of 45% of the time per year. One common finding we share with their 33-year storm occurrence record is that of reduced precipitation during JJA, with JJA found as a 3-month relative minimum in our record (that time period being associated with an enhanced Azores high and large-scale subsidence).

In terms of instrument sampling differences, monthly accumulations indicate the tendency for the PARS (gray bars) to underestimate the 2DVD (purple bars) precipitation totals in the May/December months associated with midlatitude cyclone passage and increased rainfall. Darker shading on Figure 3a indicates the precipitation contributions from the Low clouds, suggesting these clouds provide a substantial contribution to the rainfall throughout the year. This result compares well with Wood et al. (2015) that suggest shallower clouds having tops <4 km (as defined by 94-GHz W band ARM cloud radar) contribute approximately 20–40% of the total precipitation for ENA. Both disdrometers record similar total rainfall during Low cloud conditions (e.g., Figure 3f). For this data set, July and November maximize the relative contribution of Low cloud precipitation to the overall monthly total.

The prominence and timing of the diurnal cycle is contingent on cloud regime (e.g., Figures 3b and 3d). Midlatitude frontal passages are expected to occur randomly throughout the day and night for an extended data set. Deep events exhibit a weak diurnal cycle, having enhanced precipitation during the morning hours (near 12 UTC) and reduced precipitation by afternoon (Figure 3d). Albeit weak, this diurnal cycle for the Deep marine precipitation is consistent with previous (larger-scale Atlantic and/or N. Atlantic composite) investigations of the diurnal cycle of global precipitation (Chang et al., 1995; Dai et al., 2007). Less surprisingly, the disdrometers observe a stronger diurnal cycle signature for the Low clouds (Figure 3b, darker shading). This Low cloud diurnal cycle suggests one (primary) peak in rainfall around 5–7 UTC. This

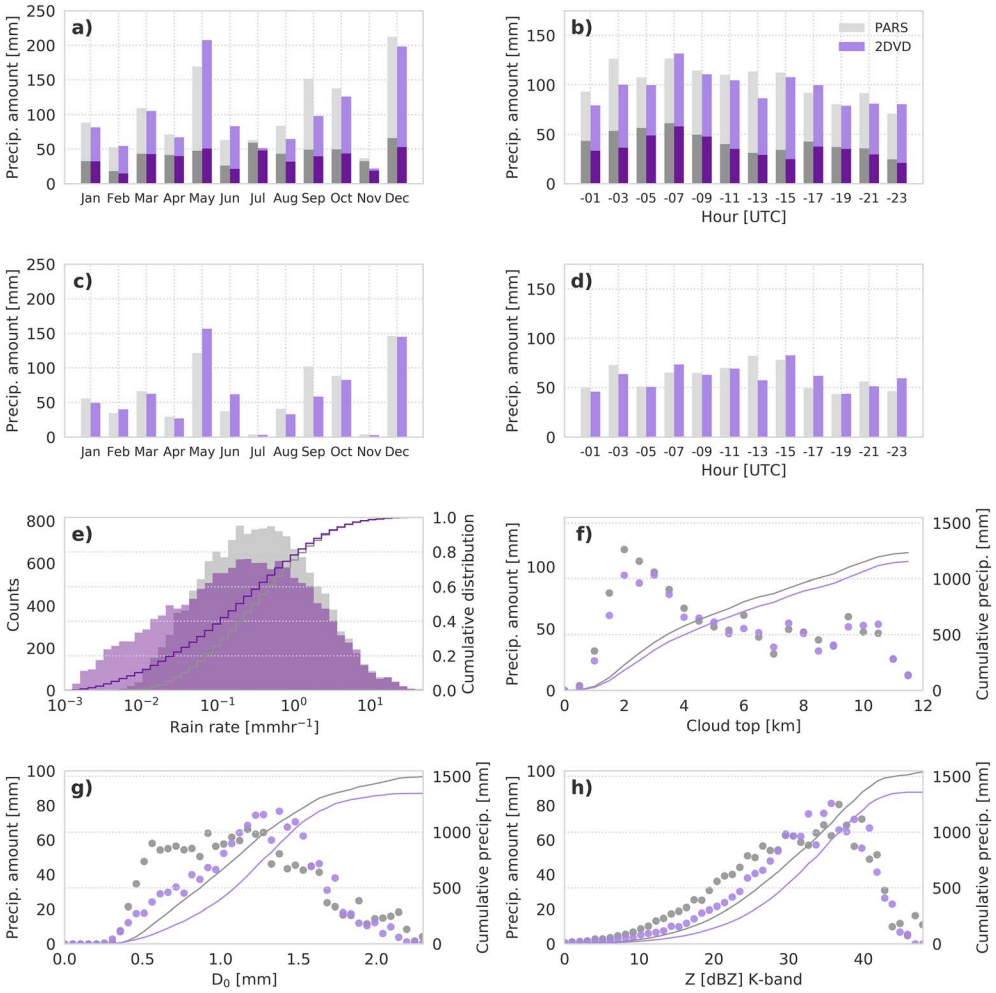

Figure 3. (a) Seasonal, and (b) diurnal cycles of precipitation from PARS (gray) and 2DVD (purple) for the Eastern North Atlantic data set. Low cloud event properties are recorded as darker shading, while Deep events are recorded with lighter shading. (c)/(d) Accumulations as in (a)/(b) but exclusive to Deep events (previous lighter shading in [a]/[b]). (e) Histograms of rain rates from the PARS and 2DVD. Lines correspond to the cumulative contribution to precipitation. Precipitation (dots) and cumulative precipitation (lines) as a function of cloud echo top height, median volume drop size (D0), and reflectivity at Ka-band are shown in (f), (g), and (h), respectively. PARS = second-generation Parsivel disdrometer; 2DVD = two-dimensional video disdrometer.

peak is similar to the first harmonic found in satellite-based liquid water path retrievals over the North Atlantic, as from Elsaesser et al. (2017, approximately 2–5 LST, see their Figure 7) and other studies of precipitation in marine regions (e.g., Rapp et al., 2013).

A secondary peak for Low cloud precipitation is observed after local noon (16 UTC), slightly closer to mid-afternoon for the 2DVD. Several studies indicate diurnal cloud and precipitation cycles are intimately linked to thermodynamic profile changes (e.g., Klein et al., 1995; Rogers et al., 1995). For example, evaporative cooling in subcloud regions from overnight stratocumulus and/or warming and decoupling of the cloud layer after sunrise impacts stability, reducing convective activity, cloud fraction, and precipitation during the morning hours. As discussed in Miller et al. (1998), this higher stability throughout the day may act to limit spontaneous convection, promoting more vigorous afternoon convection. The midafternoon peak is also reminiscent of a secondary maximum in precipitation observed for trade cumulus in the Rain in Cumulus Over the Ocean field campaign (Snodgrass et al., 2009). Their ideas may help explain the midafternoon precipitation peak over the island we observe for Low cloud events (Figure 3b).

PARS and 2DVD data sets are also partitioned as a function of rainfall rate (Figure 3e) and cumulative rainfall as a function of ETH (Figure 3f). Overall, the 2DVD samples to a higher and lower range of rainfall rates,

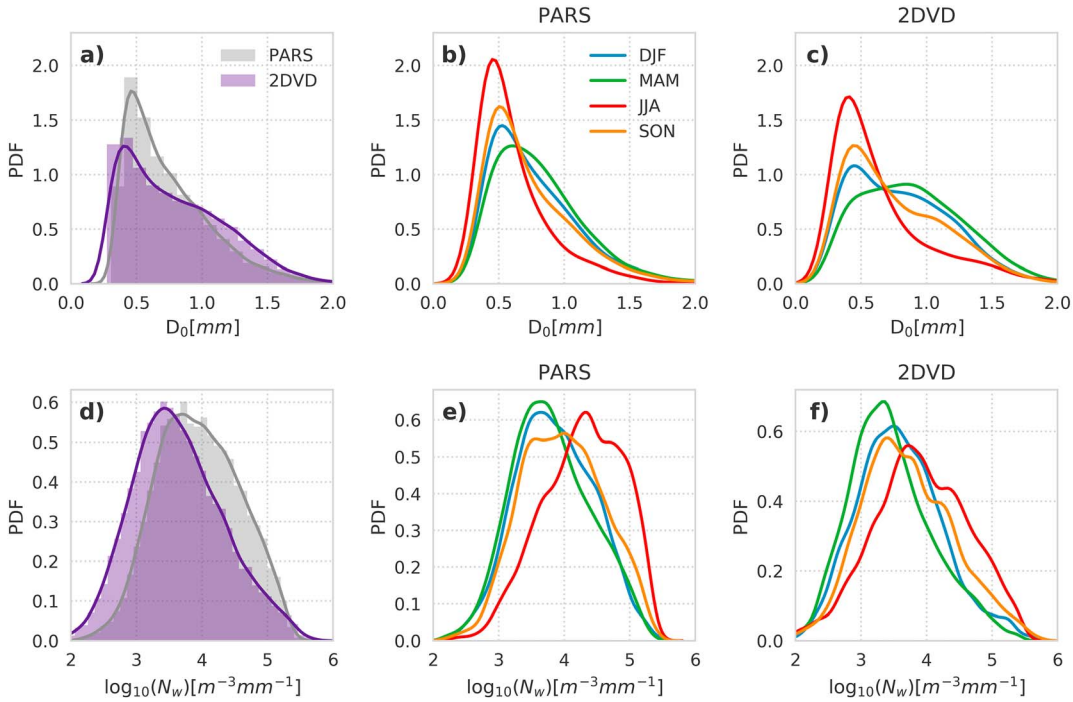

Figure 4. *D*0 and log10(*Nw*) distributions for every raindrop size distribution in the Eastern North Atlantic data set (a, d) and for different seasonal breakdown (as indicated by different colors) in (b), (c), (e), and (f). PARS = second-generation Parsivel disdrometer; 2DVD = two-dimensional video disdrometer; PDF = probability density function; DJF = December–February; MAM = March–May; JJA = June–August; SON = September–November.

recalling that both instruments are recording the same 5-min DSDs for these comparisons. Following the results in Figure 3d, the discrepancies between the PARS and 2DVD appear greater in terms of the contribution of deeper clouds to the total precipitation. Specifically, the 2DVD records approximately 100 mm of additional precipitation associated with Deep cloud events. Again, this offset may be influenced by regime-specific sampling limitations, for example the representativeness for the frequency of Deep events (e.g., May, December). Overall, the disdrometers indicate that Low cloud precipitation (ETH < 4 km) accounts for approximately 45% of the data set rainfall. This relative contribution is higher than reported for low clouds (19–36% contribution to the total precipitation from clouds with tops < 5 km) over oceanic regions as based on satellite retrievals (e.g., Elsaesser et al., 2010). These differences may represent true differences between the tropics and the midlatitudes/subtropics, as well as those caused by associated satellite retrieval and/or instrument sensitivity uncertainties compared to ground observations.

Additional breakdowns are provided for the total precipitation as a function of the surface median drop diameter *D*0 (Figure 3g) and radar reflectivity factor Z (at Ka-band radar wavelength, Figure 3h). Although the cumulative data set rainfall behaviors are similar, these plots help identify where known disdrometer sampling discrepancies may lead to differences in radar hydrological applications (e.g., possible Z-R relationships, relative radar miscalibration checks, etc.). For example, although the PARS estimates a similar total rainfall as the 2DVD over the complete data set, the instrument attributes higher rainfall accumulations to smaller *D*0 and/or lower Z DSDs, offset by reduced rainfall (total accumulation) to larger *D*0 and/or higher Z DSDs.

4.2. Additional Seasonal and Rainfall Rate DSD Comparisons

In Figure 4, we provide histograms for single parameter *D*0 and Nw quantities from the disdrometer DSDs, segregated also by seasonal breakdowns (e.g., December - February DJF, March - May MAM, JJA, and September-November SON). Seasonally, it is not surprising that JJA is the most consistent with MBL cloud/warm rain characteristics, favoring significantly higher number concentrations and smaller drop sizes. Other seasonal characteristics are similar, with MAM/DJF recording larger drop sizes associated

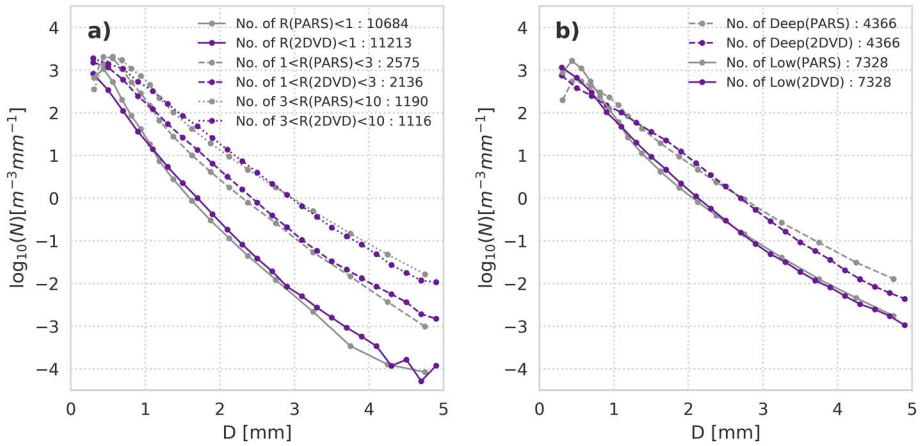

Figure 5. Mean drop size distribution plots from the PARS (gray) and the 2DVD (purple) for different rain rate intervals: $R < 1$ mm/hr, $1 < R < 3$ mm/hr, and $3 < R < 10$ mm/hr (a) and Low and Deep events (b). PARS = second-generation Parsivel disdrometer; 2DVD = two-dimensional video disdrometer.

with increased frequency of frontal passages. The 2DVD samples a wider range for the DSD parameters (Figures 4a,d), as anticipated from previous disdrometer intercomparisons (e.g., Battaglia et al., 2010; Gatlin et al., 2015; Park et al., 2017). For example, the relative peak in PARS $D0$ observations (Figure 4a) is attributed to reduced PARS sensitivity at the smaller drop sizes (first two PARS bins contain no data) and associated quantization errors when assigning smaller raindrops into larger bins. These sampling differences help explain the artificial inflation of the PARS $D0$ and Z quantities (under similar rainfall rate intervals) during lighter rainfall when compared to 2DVD measurements. Again, this increased rainfall is offset in the cumulative data set rainfall accumulations owing to the poorer performance of the PARS in heavier rainfall (e.g., Tokay et al., 2013).

Figure 5a highlights sampling differences under similar rainfall rate conditions using average DSDs as a function of rainfall rate interval for the PARS and 2DVD ($R < 1$ mm/hr, $1 \leq R < 3$ mm/hr; $3 \leq R < 10$ mm/hr). The average DSDs for our Low and Deep classifications are plotted in Figure 5b, as likely associated with lighter and heavier rainfall, respectively. At lower rainfall rates, the PARS relatively overestimates select smaller drop concentrations, as consistent with our previous statements. At higher rainfall rates, the 2DVD sampling favors increasingly higher drop concentrations for diameters $1 < D < 3$ mm, in agreement with the higher $D0$ and Z values as noted for Figure 3. In addition, higher rainfall rates and Deep events suggest that the PARS relatively overestimates the number of larger drops ($D > 3$ mm). The alignment between the instrument averages from smaller to larger drop sampling is consistent with previous PARS/2DVD comparisons (e.g., Park et al., 2017; Tokay et al., 2013).

4.3. Relationships Between Previous Global Disdrometer Deployments and Cloud Regime Characterizations

Numerous disdrometer data sets have expanded the archive of detailed, quantitative precipitation characteristics into remote global environments, strengthening opportunities for cloud process studies in support of global climate model improvement (e.g., Dolan et al., 2018; Giangrande, Bartholomew, et al., 2014; Leinonen et al., 2012; Thompson et al., 2015; Wang et al., 2018). Several efforts focus on surface-based DSD regime classifications to isolate convective clouds and processes (typically, higher drop concentrations) from stratiform (typically, smaller drop concentrations), as introduced by Bringi et al. (2003, 2009) predominantly in Darwin, Australia, for maritime continental deeper convective system contexts. Recent global summaries (Dolan et al., 2018) attempt to incorporate a wider range of cloud types and physical process implications to multiparameter DSD subsets.

Following several previous studies, we plot and contrast the ENA disdrometer DSD data sets in terms of Nw-$D0$ (Figure 6a) and LWC-$D0$ (Figure 6b) cumulative density plots. Color contours on Figure 6 correspond to the 2DVD observations, whereas the line contours correspond to the observations from the PARS. Similar to observations from Figure 3, the 2DVD shows a wider range of smaller and larger DSD

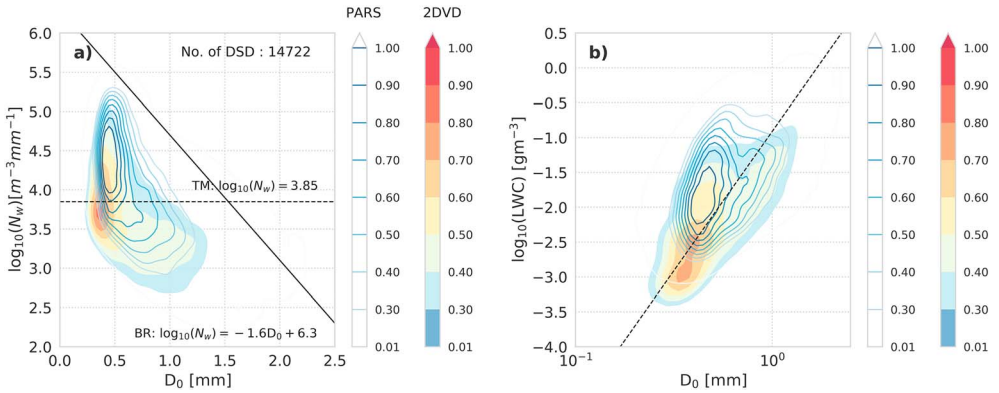

Figure 6. Two-dimensional histogram of (a) log10(*Nw*) versus *D*0 and (b) *LWC* versus *D*0 from the PARS (line contours) and the 2DVD (color contours). The convective-stratiform regime segregation criteria as from Bringi et al. (2003, BR) and Thompson et al. (2015, TM) are marked as the solid black line and dashed black lines, respectively. PARS = second-generation Parsivel disdrometer; 2DVD = two-dimensional video disdrometer; DSD = raindrop size distribution; LWC = liquid water content.

samples that encapsulates the PARS measurements. The solid line on Figure 6a corresponds to a convective-stratiform segregation line developed for maritime continent convective clouds using disdrometer measurements as proposed by Bringi et al. (2003). Although ENA samples deep convective clouds, few ENA DSDs share characteristics with the more intense (convective core) maritime convective clouds and their precipitation, with the majority of the ENA DSDs as those that residing to the right (stratiform side) of this line. The dashed lines on Figure 6 correspond to a proposed "oceanic" cloud convective-stratiform segregation, following Thompson et al. (2015) for a wider range of tropical convection over ARM Manus and Gan Island deployments. From Thompson et al. (2015), DSDs that reside above these dashed lines correspond to "convective" cloud DSDs in oceanic regimes. Overall, we note that shallower and/or weaker convective clouds found at ENA arguably promote less pronounced separations in DSD characteristics. However, there are discrepancies between the PARS and 2DVD sampling, with the PARS favoring larger drop sizes, number concentrations, and higher LWC for similar DSDs. Interestingly, ENA DSD data sets are unique for global compilation studies (e.g., Dolan et al., 2018) in terms of their relatively small *D*0 values, especially if compared to previous midlatitude deployments. Moreover, ENA data sets reside to the left of these depictions and similar to the light rain, smaller-drop periphery of the DSD characteristics shown for higher and lower latitude conditions and/or shallower-topped clouds (Dolan et al., 2018).

DSD parameters are separated in terms of Low and Deep classifications (Figure 7) as a reference for relative disdrometer performance under these cloud conditions. The radar-defined Low (Figures 7a and 7b) and Deep (Figures 7c and 7d) DSD properties align well with previous Thompson et al. (2015) separations for oceanic convective and stratiform conditions. Although the specifics of their proposed separation may be sensitive to processing or other instrument factors, ENA disdrometers conceptually support this form of oceanic breakdown for predominantly nonoverlapping ENA Low and Deep DSD populations. When comparing disdrometer units, the 2DVD typically samples the more pronounced stratiform behaviors for this data set, corresponding typically to larger drop sizes for Deep cloud DSDs and smaller drop sizes for Low cloud DSDs.

As previously reported, lower clouds are associated with approximately 45% of the total precipitation. The Low cloud precipitation also accounts for approximately two thirds of the total DSDs sampled (7,328 and 4,366 DSDs, respectively), with the majority of DSDs favoring relatively higher concentrations of small drops. Similarly, the Low cloud DSDs indicate a substantial contribution from very light rain that is close to the lower sampling limits of these disdrometers. Satellite cloud radars (i.e., CloudSat) and passive microwave applications should be sensitive to these conditions (e.g., Miller & Yuter, 2013; Stephens et al., 2002) for future comparison. However, this high frequency of smaller drop DSDs as in Figures 6 and 7 may explain some of the discrepancy in total rainfall between ground and longer wavelength radar-based satellite estimates for these regions. Note again, these disdrometer observations are not sampling classical drizzling

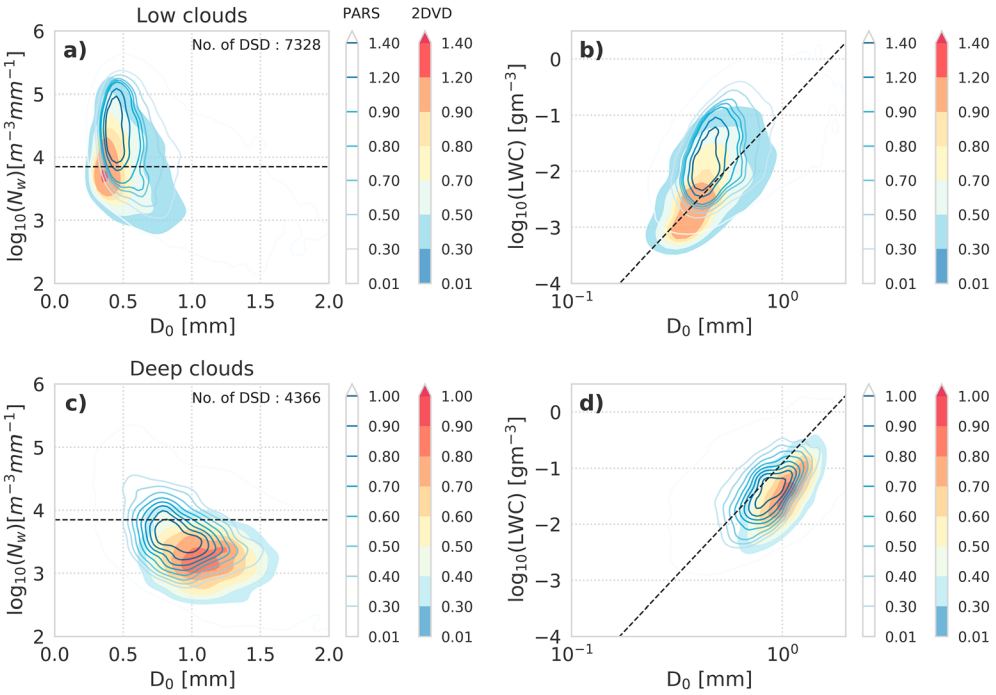

Figure 7. As in Figure 6, for Low clouds (a, b) and Deep clouds (c, d). PARS = second-generation Parsivel disdrometer; 2DVD = two-dimensional video disdrometer; DSD = raindrop size distribution; LWC = liquid water content.

conditions at ENA (e.g., Thurai et al., 2017). Thus, we also suggest these conditions strongly argue for future instrument collocation for complete drizzle and light rain sampling (e.g., Bringi et al., 2018; Thurai et al., 2017), as very light rain conditions (e.g., $R < 5$ mm/hr in midlatitude or continental disdrometer efforts) are often removed or deemphasized as less important to the total rainfall, which is clearly not the case over the ENA.

5. Low Cloud Precipitation: Relationships With Cloud Properties, Subcloud Environment

Although light rain and shallow cloud precipitation (e.g., $R < 3$ mm/hr) is often overlooked in disdrometer-based studies, the previous sections illustrate that these conditions may carry a significant contribution to the total precipitation accumulation at ENA. The following sections place additional emphasis on Low cloud precipitation and several DSD controls therein. Based on our intercomparison of ENA disdrometers, the authors suggest that 2DVD performance was comparable to the PARS over the extended ENA record and potentially offers sampling improvements under lighter rain conditions useful for designating changes in mean/median drop size. Therefore, we will limit our attention to 2DVD measurements for the remainder of our Low cloud precipitation analyses.

5.1. The 2DVD Rainfall Rate-Reflectivity Factor Relationships

In Table 1, we summarize rainfall rate R versus reflectivity factor Z relationships derived from the cumulative 2DVD disdrometer data set for select cloud breakdowns. The empirical $R(Z)$ rainfall relations are fit using standard methods from 2DVD data sets according to the form $Z = aR^b$, where Z (linear) is in mm^6/m^3, R is in millimeter per hour, and a and b are constants. As one method to align comparisons across various behaviors, a similar (although less optimal) fit was performed assuming a fixed b coefficient exponent, $b = 1.4$. The value of this exponent is the same as the value associated with the operational Next Generation Weather Radar network (Fulton et al., 1998) but also falls within the wider ENA data set range for rain we report in Table 1.

Although disdrometer sampling does not capture pure drizzling cloud conditions (e.g., as reported by Comstock et al., 2004), the estimated empirical relationships (including fixed b coefficient examples) favor

Table 1
Radar Rainfall Relations for the Eastern North Atlantic Two-Dimensional Video Disdrometer Data Set

Wavelength	All (10,321)	Low (5,831)	Deep (4,492)	Low, *RH* > 90% (1,984)	Low, *RH* < 90% (3,851)	Low, *ETH* < 2 km (2,035)	Low, *R* > 0.5 mm/hr (1,865)	Low, *R* < 0.5 mm/hr (3,966)
X band	$Z = 162R^{1.9}$	$Z = 133R^{1.9}$	$Z = 201R^{1.8}$	$Z = 107R^{1.9}$	$Z = 152R^{1.9}$	$Z = 141R^{1.8}$	$Z = 127R^{1.8}$	$Z = 669R^{2.0}$
Ka band	$Z = 411R^{1.2}$	$Z = 293R^{1.3}$	$Z = 424R^{1.2}$	$Z = 153R^{1.5}$	$Z = 263R^{1.4}$	$Z = 197R^{1.5}$	$Z = 231R^{1.4}$	$Z = 861R^{2.0}$
Fixed *b* coefficient = 1.4								
X band	$Z = 309R^{1.4}$	$Z = 238R^{1.4}$	$Z = 347R^{1.4}$	$Z = 201R^{1.4}$	$Z = 250R^{1.4}$	$Z = 185R^{1.4}$	$Z = 231R^{1.4}$	$Z = 326R^{1.4}$
Ka band	$Z = 286R^{1.4}$	$Z = 237R^{1.4}$	$Z = 304R^{1.4}$	$Z = 185R^{1.4}$	$Z = 263R^{1.4}$	$Z = 229R^{1.4}$	$Z = 231R^{1.4}$	$Z = 445R^{1.4}$

Note. Table includes cumulative data set relationships, as well as those for Low clouds having *ETH* < 4 km, Deep events having *ETH* > 4 km, Low clouds with below cloud base RH greater/less than 90%, Low clouds with *ETH* < 2 km, and Low clouds with *R* greater/less than 0.5 mm/hr. Coefficients estimated at X-band (3-cm) and Ka-band (8-mm) wavelengths ($T = 20°$). ETH = echo top height; RH = relative humidity.

relatively small values of the a coefficient. Lower a coefficients are typically indicative of higher concentrations of smaller drops, and this suggests the prevalence of small drops at ENA, compared to the wealth of previous rainfall studies having similar b coefficients. Table 1 includes additional coefficient breakdowns that isolate the changes in shallow cloud relationships for lower cloud base and/or higher subcloud *RH* (or pressure) conditions. In all breakdowns, more restrictive low cloud or less favorable evaporation conditions typically favor relationships having the smallest coefficients (a coefficients between 100 and 200). Nevertheless, these coefficient values are still substantially larger than drizzle relations reported by Comstock et al. (2004), wherein those relationships were developed using vertically pointing, shorter-wavelength radar estimates of Z (35 GHz, Ka band) coupled with in situ drizzle sampling using methylene blue filter paper (a coefficients $\approx$ 50 and $b \approx 1$). For completeness, Table 1 includes a cumulative ENA data set relationship and a matched relationship for Deep conditions. In these examples, cumulative and Deep cloud conditions report empirical fit coefficients more in line with widespread stratiform rainfall studies from previous ARM midlatitude convective and/or Amazon tropical X band efforts (e.g., Giangrande, Collis, et al., 2014; Wang et al., 2018).

5.2. DSD Quantity Relationships With Low Cloud Properties

Studies have also explored the relationships between ENA cloud properties, the propensity for low clouds to drizzle, and the depth of the subcloud virga layer (e.g., Yang et al., 2018). In a complementary fashion, this ENA study investigates the potential connections between the surface precipitation and Low cloud DSD properties, the subcloud environment, and other controlling factors. Partially, this is motivated by the physical expectation that thicker or deeper MBL clouds promote greater in-cloud collisional growth (e.g., Kostinski, 2008) and therefore larger droplet sizes and precipitation rates. This behavior is consistent with observations in marine stratocumulus (Pawlowska, 2003; vanZanten et al., 2005; Wood, 2005). Larger surface median drop sizes may also be promoted by lower subcloud relative humidity *RH* (smaller drops being evaporated relative to larger drops), as well as subcloud drop collisional growth.

In Figure 8, we plot a two-dimensional histogram for several DSD quantities of interest as a function of the cloud base and cloud thickness. As previously alluded, the majority of samples (e.g., Figure 8h) are associated with Low clouds having their ETH below 4 km (solid black line) and cloud bases below 2 km. As the cloud thickness increases, there is an increase in all DSD parameters ($D0$, R, *LWC*, Z, and a scanning dual-polarization radar differential reflectivity factor *ZDR* reference as estimated from the DSDs). This behavior spans the transition from MBL to deeper clouds and is consistent with more intense rainfall and/or larger drop sizes accompanying thicker clouds. To better understand the dependence on cloud base height within the lower cloud category, we look to mean drop volume diameter $D0$ (Figure 8a) and the subcloud *RH* (Figure 8d).

For a given cloud base height, Z, *ZDR*, and $D0$ increase with cloud thickness, as expected. For a given cloud thickness, these quantities typically also increase with increasing cloud base. In both cases, the observations suggest these relationships as most pronounced for shallower cloud properties. Mean R and *LWC* quantities demonstrate similar association with these cloud properties, with deeper clouds generally favoring higher *LWC* and R. In the case of *ZDR* (Figure 8f), this quantity is estimated from the 2DVD disdrometer (as ARM operates a dual-polarization scanning Ka-band radar at ENA), but the range of values for MBL

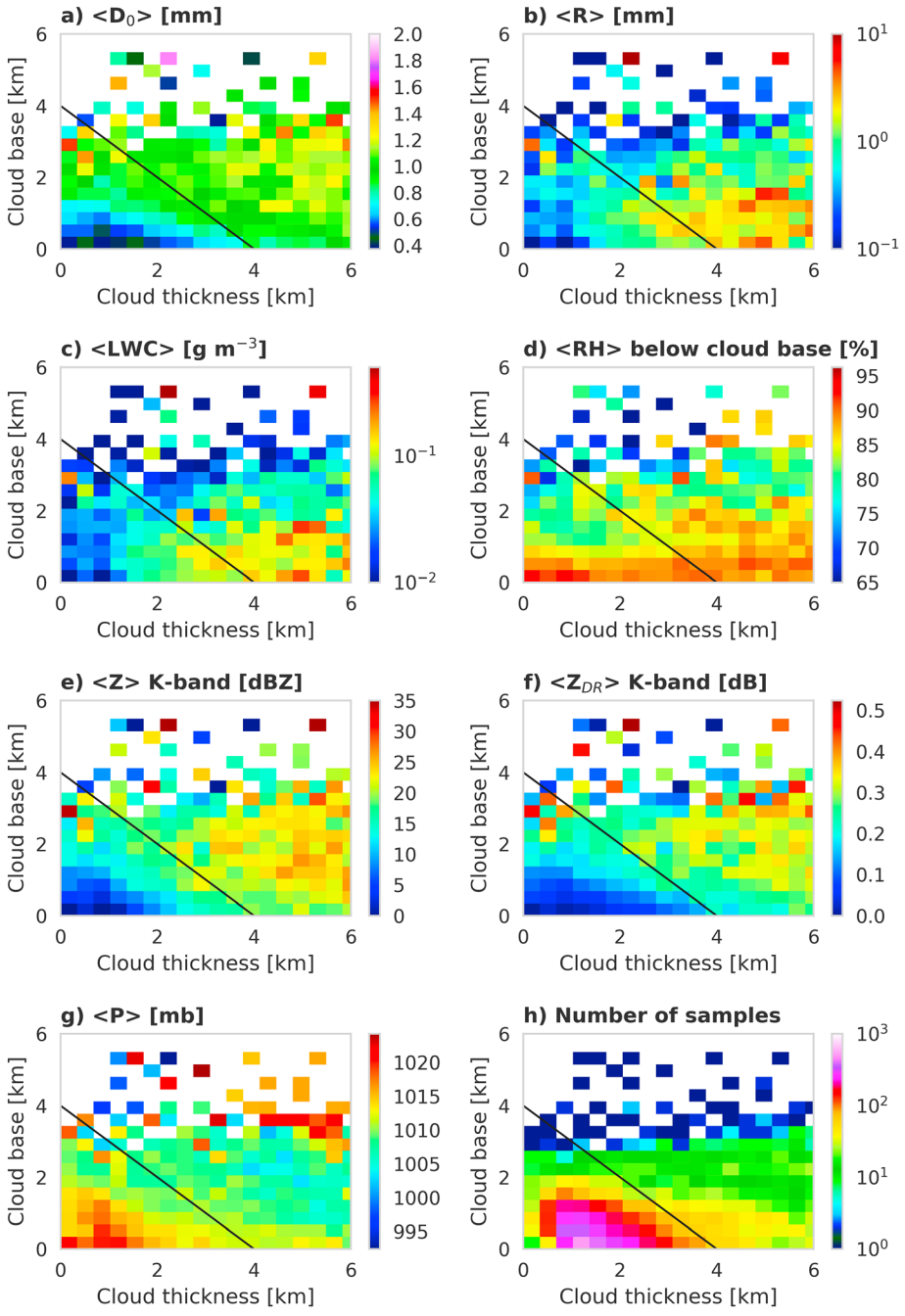

Figure 8. Two-dimensional histogram for mean values of (a) *D*0, (b) *R*, (c) *LWC*, (d) relative humidity (RH) below cloud base, (e) Ka-band *Z*, (f) Ka-band *ZDR*, and (g) surface pressure *P* as a function of cloud base and thickness. The number of samples for each histogram bin is recorded in (h). Our Low/Deep cloud segregation is shown as a solid black line in each plot. LWC = liquid water content; RH = relative humidity.

clouds (0.1–0.2 dB) is within the margin of typical radar miscalibration offsets. Note, the progression toward thicker clouds suggests only limited scanning dual-polarization radar usefulness (*ZDR* below approximately 0.5 dB). Interestingly, the *Z* field (Figure 8e) also indicates larger surface mean *Z* for higher cloud base MBL events (approximately 5- to 10-dBZ spread). Although larger *D*0 values for higher cloud base is consistent with evaporation arguments (lowering of *RH* below higher base MBL clouds in well-mixed subcloud layers), the larger mean *Z* values (for similar thickness) suggests additional or larger drops (with $Z \approx ND^6$) with increasing cloud base (echoed in *R* and *LWC* averages). Physically, the behavior could be attributed

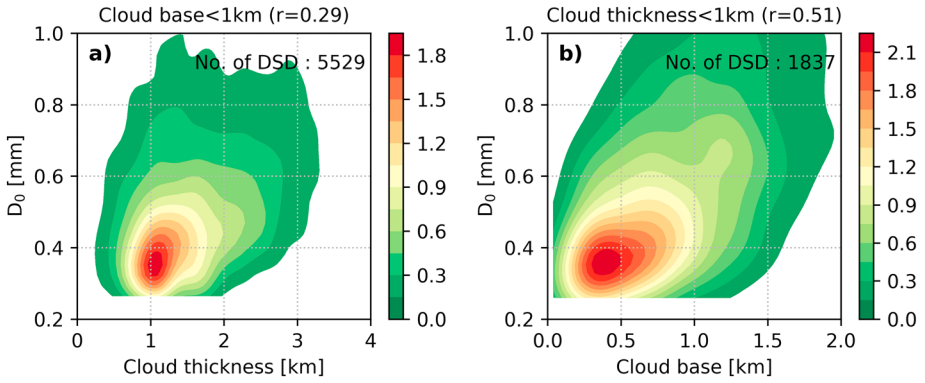

Figure 9. Two-dimensional histogram of *D*0 versus cloud thickness for (a) Low clouds with cloud base <1 km and (b) *D*0 versus cloud base for Low clouds with cloud thickness <1 km. DSD = raindrop size distribution.

to enhanced collision-coalescence process accompanying higher cloud bases. Subcloud rain processes were not modeled for this study, but we do not anticipate collision-coalescence processes operating over these 1- to 2-km layer differences to explain this increase in *Z* in the subcloud layer.

Larger-scale synoptic wave passages that promote thicker or higher-based clouds are suspected as those conditions are associated with the observed changes in surface rainfall quantities. Under this argument, lower values of surface pressures associated with prefrontal conditions may promote deeper clouds, as well as enhanced low clouds. Initially, this possibility is corroborated by the average surface pressure (Figure 8g), which suggests a sharp gradient within the Low cloud averages (below/above ETH and/or cloud bases around 2 km). These lower pressures are coupled with thicker or higher-based MBL or shallow clouds, and enhanced *D*0, *Z*, and *ZDR* conditions. The pressure distribution in Figure 8 suggests two distinct subregimes making up the Low cloud category: (i) the classical subtropical stratocumulus regime characterized by high-pressure, low cloud bases, and thin clouds and (ii) deeper clouds, with cloud tops still below 4 km, accompanying lower surface pressures likely symptomatic of influences from synoptic-scale forcing.

Joint distributions of median drop size *D*0 versus Low cloud thickness (for cloud base height < 1 km) and Low cloud base height (for cloud thickness < 1 km) are provided in Figures 9a and 9b, respectively. Cloud thickness shows a weak positive correlation with *D*0 ($r \sim 0.3$, Figure 9a), suggesting that the thicker clouds are slightly associated with larger drop sizes at the surface. For similar cloud thickness, the *D*0 is better correlated with cloud base height ($r \sim 0.5$, Figure 9b), as are the mean radar quantities (not shown). As noted, attributing physical process arguments to these results is unsatisfying given the possible synoptic wave influence on Low clouds. It should be mentioned that previous studies (e.g., Comstock et al., 2004; vanZanten et al., 2005) report that drizzle rates are strongly controlled by variations in drizzle drop number rather than variations in drop size. For light rain events, we did not observe a strong surface relationship between Low cloud *R* and *D*0 ($r \sim 0.5$), but rainfall relations (e.g., Table 1) show a modest range of *b* coefficient values that suggests drop size variability is more important to rainfall rate than for weaker drizzle rates.

6. Low Cloud Precipitation: Relationship to Large-Scale Controls

The diurnal cycle and larger-scale (variability associated with synoptic waves) work in concert to modify cloud and precipitation properties. The ENA site is located in the midlatitudes and is characterized by substantial multiday variability in synoptic configuration, stability, and cloud properties (e.g., Naud et al., 2018). Using the technique of self-organizing maps, Mechem et al. (2018) found significant influences of synoptic systems over the ENA, even in June when the lower tropospheric flow is, on average, dominated by the Azores High. Of particular interest is their pretrough state, which occurs 40% of the time and is characterized by southerly or southwesterly flow at the surface. In this pretrough state, the Azores lie directly along the transition of the large-scale vertical velocity from upward and downward motion (their Figure 6). Furthermore, Mechem et al. (2018) show that these synoptically forced states (that is, the pretrough and trough states associated with large-scale ascent nearby or over the Azores) are typically accompanied by

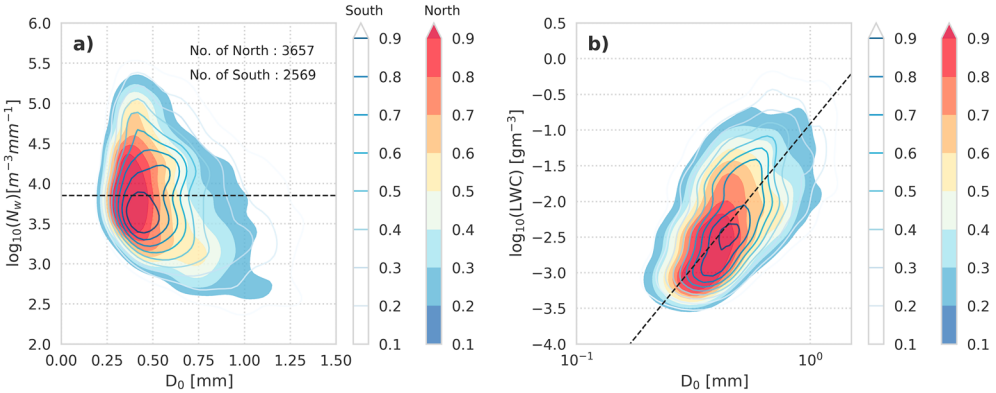

Figure 10. Low cloud 2-D histogram of (a) log10(*Nw*) versus *D*0 and (b) *LWC* versus *D*0 from the two-dimensional video disdrometer for northerly (shaded contours) versus southerly (line contours) winds. The convective-stratiform regime segregation criteria as from Thompson et al. (2015) is marked as the dashed line. LWC = liquid water content.

winds from the south or southwest and by cloud properties with greater amounts of vertically integrated condensate. Their result strongly suggests that such enhancements in cloud thickness and potential for precipitation are a result of synoptic influences.

The synoptic influences on low cloud precipitation may be considered in a simplified manner by examining observed precipitation properties as a function of wind direction (as in Figure 2). In Figure 10, we plot the DSD joint *Nw*-*D*0 and *LWC*-*D*0 histograms (from the 2DVD) for Low clouds having 850-mb winds from northerly and southerly directions (3,657 and 2,569 DSDs, respectively). The shaded regions correspond to the northerly wind DSD observations, and the line contours correspond to the southerly flow observations. The most noticeable transition associated with wind direction is the shift found for southerly flows toward DSDs favoring larger *D*0 for similar values of *Nw* and *LWC*.

Diurnal cycle (accumulation) plots (Figure 11) corroborate the precipitation enhancement observed under southerly flows. DSDs collected during prevailing southerly flows are associated with a higher total precipitation accumulation for this data set than northerly flows, and this accumulation is associated with a smaller number of DSD observations. This indicates that southerly flows must also be associated with the higher precipitation rates (as compared to northerly flows). Southerly flows exhibit a characteristic early morning peak and depression after sunrise (Figure 11b), but the behavior is less pronounced compared to the northerly or westerly directions (Figures 11a and 11c). A less pronounced diurnal cycle likely suggests additional influence of frontal (random) precipitation contributions.

Northerly and westerly Low conditions demonstrate the characteristic diurnal cycle found in marine stratocumulus regimes. In marine stratocumulus, the strongest precipitation occurs over the predawn hours when net cloud top radiative cooling is strong and the cloud is thickest (e.g., Burleyson et al., 2013). The northerly and westerly conditions also suggest a midafternoon rainfall increase as previously documented (e.g., Miller et al., 1998). In Figure 11, we include the diurnal cycle for the average cloud thickness and cloud base. Northerly flows exhibit the thinnest clouds, though with a period of larger cloud thickness in the predawn hours associated with the maximum in precipitation typical of radiatively driven MBL clouds. Specifically, the cloud base rises and the cloud thins after sunrise. Southerly and westerly flows demonstrate thicker clouds. Overall, cloud base behaviors are generally consistent with northerly flows favoring shallower boundary layers, thinner clouds, high surface pressure, stronger stability, and large-scale subsidence (Mechem et al., 2018). In short, textbook stratocumulus-topped boundary layers likely occur predominantly during northerly flows. In contrast, southerly flows likely correspond to a more westward positioning of the Azores high (lower values of surface pressure over ENA), which acts to reduce subsidence (or provide upward vertical motion) over the site and promote enhanced cloudiness via a greater influence of poleward synoptic systems.

As reported by Mechem et al. (2018), southerly wind patterns are those associated with prefrontal trough placements and also those more associated with thicker clouds. At present, previous cloud radar-based

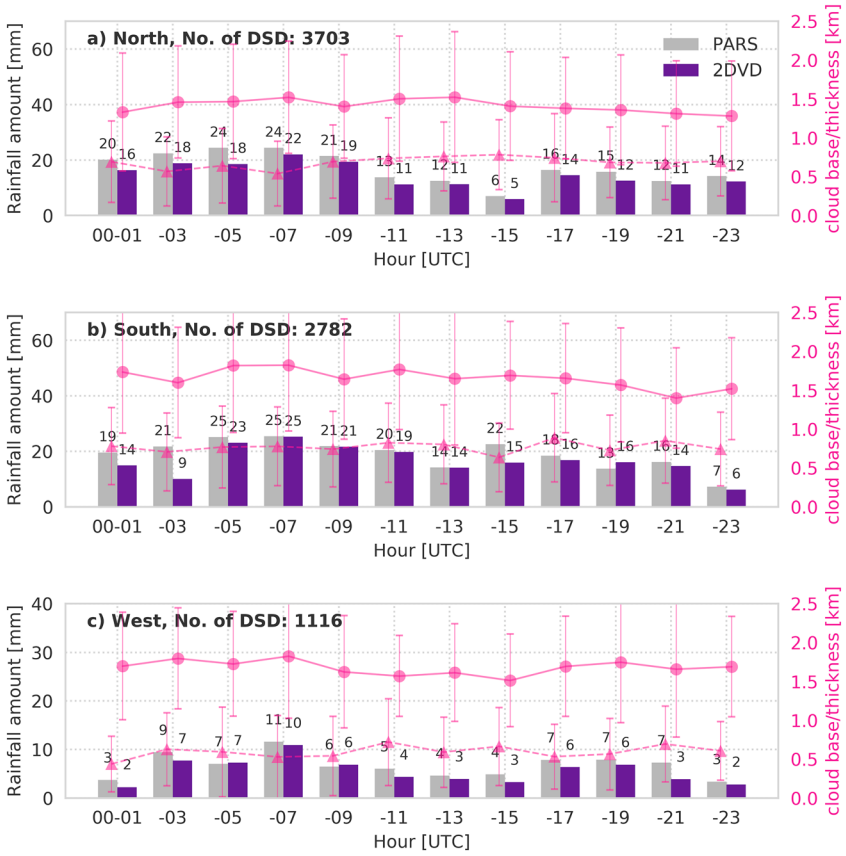

Figure 11. Diurnal cycle of precipitation from PARS and 2DVD for Low clouds contingent on the ambient wind directions: (a) northeasterly, (b) southerly, and (c) westerly. Cloud base (triangles) and cloud thickness (circles) are also plotted (mean and standard deviation). Numbers above each bar are the associated rainfall amounts. PARS = second-generation Parsivel disdrometer; 2DVD = two-dimensional video disdrometer; DSD = raindrop size distribution.

definitions for MBL clouds (relying primarily on ETH or similar) inevitably include prefrontal or otherwise synoptically forced low cloud events that produce enhanced cloud thickness and precipitation rates. Overall, the larger values of surface precipitation and cloud thickness accompanying southerly flows (Figures 8 and 11) strongly suggest that these cases are synoptically enhanced by large-scale ascent. This would be expected for deepening boundary layers in advance of frontal passage (those also favoring enhanced Z, ZDR, and $D0$ conditions).

To explore the possible larger-scale enhancement further, we show that the cloud thickness, surface rainfall rate R and median drop size $D0$ are strongly associated with the larger-scale flow when coupled with the surface pressure (as proxy for possible frontal passage, Figure 12). Following the average lower cloud pressure characteristics (Figure 8g), we set an additional criterion to only consider the Low cloud precipitation measurements having $ETH < 2$ km (to further mitigate questionable low clouds from MBL cloud DSDs). In terms of cloud thickness, we observe that the thicker clouds are typically associated with lower surface pressure, with a bimodal behavior for southerly flows. This bimodality is suggestive of one higher pressure MBL cloud regime (typical, Azores high) and one lower pressure MBL cloud regime likely associated with prefrontal/postfrontal passage. We also observe a significant enhancement in the rainfall and $D0$ characteristics associated with southerly flows and their coupling with lower surface pressure. These patterns tend to confirm that even if controlling for relatively shallow-topped low cloud examples in attempts to isolate MBL cloud behaviors, we find subsets of enhanced cloud thickness and surface precipitation properties as arguably linked with larger-scale conditions (proximity to frontal passage).

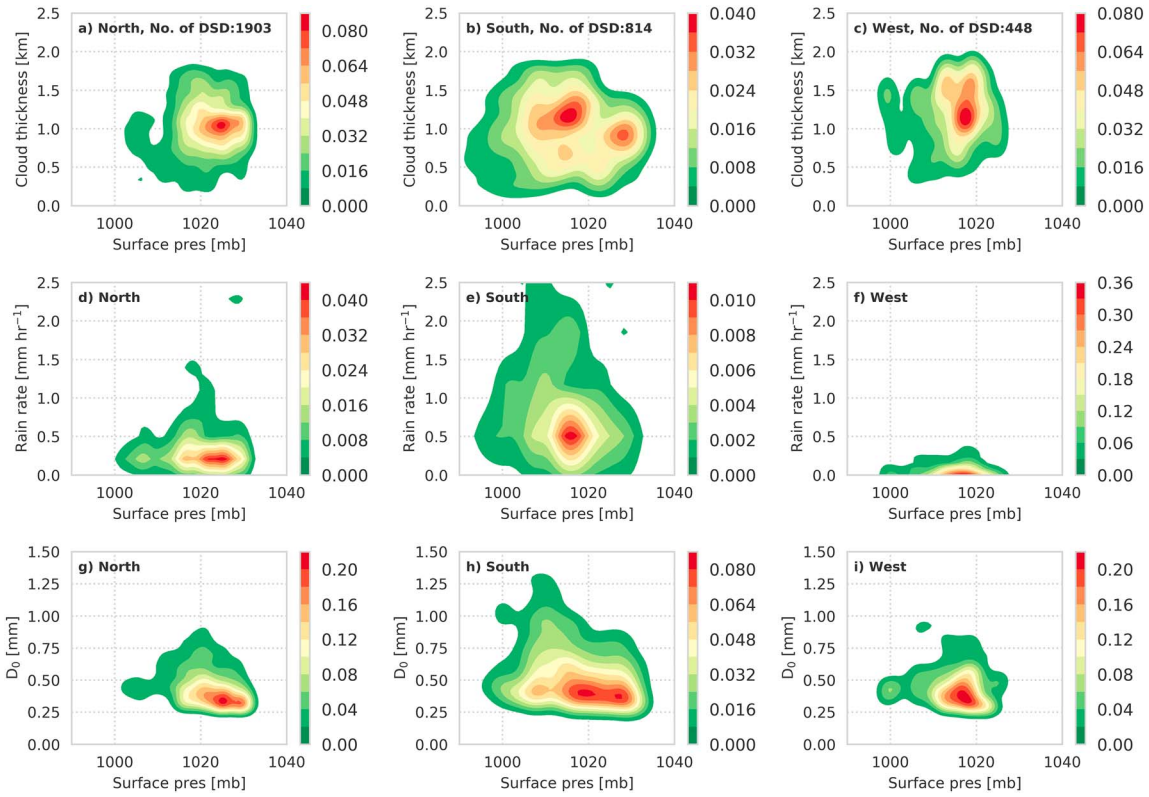

Figure 12. Two-dimensional histograms of cloud thickness (a–c), rainfall rate (d–f), and *D*0 (g–i) versus surface pressure for a subset of the Low clouds (*ETH* < 2 km). Breakdowns are contingent on the ambient wind direction: northeasterly (a, d, g), southerly (b, e, h), and westerly (c, f, i). DSD = raindrop size distribution.

7. Discussion and Summary

This study presents the precipitation properties for oceanic-type cloud conditions as sampled by the ARM ENA observatory for a multiyear period. Owing to its extended record and unique global placement in a transitional region between the midlatitudes and subtropics, these observations provide a valuable reference for global precipitation that is heavily influenced by shallow clouds. Initial results show relative Northern Atlantic diurnal precipitation behaviors similar to available global satellite precipitation standards. However, measurements at ENA indicate higher fractional contributions from marine, low clouds to rainfall totals (45%) when compared with satellite precipitation estimates, which may be the result of improved surface sampling methods into lighter rainfall conditions than current satellite techniques.

Sampling capabilities for two types of disdrometers were considered by this study. The authors suggest that the improved sensitivity of the 2DVD to smaller drop sizes yielded better lighter rain records for analysis, but both the PARS and 2DVD perform to within 10% for rainfall accumulations and suggest similar diurnal and annual precipitation cycles for ENA clouds. For lower cloud and/or lighter rainfall rate <3-mm/hr comparisons, the 2DVD typically samples fewer drops but records a wider diversity of drop sizes. The PARS estimates lower rainfall totals in heavier rain contexts, as was associated in part with lesser sampling capabilities for larger drop sizes (both in heavier and lighter rain instances). Both disdrometers recorded smaller median drop sizes than have been typically reported for midlatitudes or other global regimes (tropics, higher latitudes) as based on previous global summaries (e.g., Dolan et al., 2018). Although deeper clouds were frequent, the ENA site did not record a significant number of heavy rainfall rate events or DSDs characteristics traditionally associated with deeper convective precipitation cores. Nevertheless, ENA data sets suggest nonoverlapping DSD behaviors between Low and Deep cloud regimes, in line with previous oceanic disdrometer-based cloud segregations proposed by Thompson et al. (2015). Overall, these results suggest caution in assuming precipitation characteristics at the ENA site are a proxy for global precipitation when based on similar frequency of cloud occurrence.

When considering possible controls on the observed precipitation for Low cloud conditions, several factors were suggested as influential to ENA surface precipitation measurements. First, cloud thickness was found to exert a minor control on the surface precipitation. In basic terms, thicker clouds are typically associated with larger drop sizes and enhanced rainfall. However, it was found that cloud base—as coupled to subcloud variability in RH or linked through joint changes in 850-mb winds and surface pressure—was arguably more important to the observed Low cloud DSD quantities. Specifically, clouds associated with the southerly flows promoted thicker clouds and enhanced DSD quantities, including larger mean rainfall rates, radar reflectivity factors, and median drop size. The diurnal cycle under these conditions was weaker, also suggesting these southerly flows and associated low clouds as influenced by frontal systems. This is contrasted with northerly or westerly flows suggesting conventional radiatively driven marine stratocumulus that exhibit a pronounced diurnal cycle in cloud thickness and precipitation.

Overall, the observational record indicates ENA as a unique precipitation testing ground at the edge of the sampling capabilities for disdrometer equipment. As a ground validation site for satellite-based retrievals, ENA may be particularly useful for capturing precipitation from shallow clouds not currently well sampled by precipitation radar on satellites. From the examples we provide (e.g., Figures 8, 11, and 12), Low clouds observed over the ENA site are highly variable and often not consistent with MBL cloud diurnal cycle expectations found in other subtropical marine cloud regions. We note that previous ENA MBL cloud studies typically avoid southerly flows to ensure classical stratocumulus conditions. This decision is often argued as a consideration to avoid possible island influences. Although we do not quantify orographic controls associated with southerly flows, we believe these efforts indicate larger-scale forcing as a significant factor on the observed surface DSD and cloud properties of Low clouds under southerly wind conditions (clouds of similar thickness/base). In this regard, larger-scale synoptic forcing may also exercise control on nonprecipitating clouds. The simple approach for characterizing the synoptic regime by flow direction taken in this study is roughly consistent with the synoptic classification analysis on the ENA region from Mechem et al. (2018). The synoptic state exerted greater control on cloud and precipitation properties than expected. This suggests, in hindsight, that a complete characterization of the synoptic state (as in Mechem et al., 2018) could have provided more insight. However, the details of the DSD precipitation and cloud properties documented in this paper invites further exploration of the data set and detailed analysis as a function of season and synoptic regime.

Acknowledgments
This paper has been authored by employees of Brookhaven Science Associates, LLC, under contract DE-SC0012704 with the U.S. Department of Energy (DOE). The publisher by accepting the paper for publication acknowledges that the United States Government retains a nonexclusive, paid-up, irrevocable, worldwide license to publish or reproduce the published form of this paper, or allow others to do so, for United States Government purposes. The authors acknowledge the Atmospheric Radiation Measurement (ARM) program, a user facility of the U. S. DOE, Office of Science, sponsored by the Office of Biological and Environmental Research, as well as support from the Atmospheric Systems Research (ASR) program of that office. This work was partially supported by the Climate Model Development and Validation (CMDV) activity funded by the Office of Biological and Environmental Research in the U.S. DOE, Office of Science. Coauthor Mechem was supported by the DOE Office of Science grant DE–SC0016522. The authors would also like to thank S. Collis and Z. Sherman (ANL) for ARM site map, plotting tools under the open-source Py-ART toolkit (Heistermann et al., 2015; Helmus & Collis, 2016).

Data Availability

All ARM data sets used for this study can be downloaded at https://www.arm.gov and associated with several "value added product" streams. Figure 1 was generated using terrain data available from the U.S. Geological Survey. These data are distributed by the Land Processes Distributed Active Archive Center (LP DAAC), located at USGS/EROS, Sioux Falls, SD. https://lpdaac.usgs.gov. The PyDSD processing codes are available through J. Hardin at https://github.com/josephhardinee/PyDSD and J. Hardin and N. Guy (2017, December) under the doi: https://doi.org/10.5281/zenodo.9991. PyTMatrix is available from J. Leinonen at https://github.com/jleinonen/pytmatrix/.

Competing Interests

The authors declare that they have no conflict of interest.

References

Albrecht, B. A., Bretherton, C. S., Johnson, D., Schubert, W. H., & Frisch, A. S. (1995). The Atlantic Stratocumulus Transition Experiment—ASTEX. *Bulletin of the American Meteorological Society*, *76*(6), 889–904. https://doi.org/10.1175/1520-0477(1995)076<0889:TASTE>2.0.CO;2

Albrecht, B. A., Jensen, M. P., & Syrett, W. J. (1995). Marine boundary layer structure and fractional cloudiness. *Journal of Geophysical Research*, *100*(D7), 14,209–14,222. https://doi.org/10.1029/95JD00827

Atmospheric Radiation Measurement (ARM) Climate Research Facility (1996). updated hourly. Active Remote Sensing of CLouds (ARSCL) product using Ka-band ARM Zenith Radars (ARSCLKAZRBND1KOLLIAS). Eastern North Atlantic (ENA) Graciosa Island, Azores, Portugal (C1). Compiled by K. Johnson, S. Giangrande and T. Toto. Atmospheric Radiation Measurement (ARM) Climate Research Facility Data Archive: Oak Ridge, Tennessee, USA. Data set accessed at https://doi.org/10.5439/1350630

Bartholomew, M. (2014). ARM's handbook for the Parsivel2 laser disdrometer, Tech. Rep., U.S. DOE, Office of Science, Office of Biological and Environmental Research.

Battaglia, A., Rustemeier, E., Tokay, A., Blahak, U., & Simmer, C. (2010). PARSIVEL Snow observations: A critical assessment. *Journal of Atmospheric and Oceanic Technology*, *27*(2), 333–344. https://doi.org/10.1175/2009JTECHA1332.1

Bony, S., & Dufresne, J. (2005). Marine boundary layer clouds at the heart of tropical cloud feedback uncertainties in climate models. *Geophysical Research Letters*, *32*, L20806. https://doi.org/10.1029/2005GL023851

Bringi, V., Thurai, M., & Baumgardner, D. (2018). Raindrop fall velocities from an optical array probe and 2-D video disdrometer. *Atmospheric Measurement Techniques*, *11*, 1377–1384. https://doi.org/10.5194/amt-11-1377-2018

Bringi, V. N., Chandrasekar, V., Hubbert, J., Gorgucci, E., Randeu, W. L., & Schoenhuber, M. (2003). Raindrop size distribution in different climatic regimes from disdrometer and dual-polarized radar analysis. *Journal of the Atmospheric Sciences*, *60*(2), 354–365. https://doi.org/10.1175/1520-0469(2003)060<0354:RSDIDC>2.0.CO;2

Bringi, V. N., Huang, G.-J., Chandrasekar, V., & Gorgucci, E. (2002). A methodology for estimating the parameters of a gamma raindrop size distribution model from polarimetric radar data: Application to a squall-line event from the TRMM/Brazil Campaign. *Journal of Atmospheric and Oceanic Technology*, *19*(5), 633–645. https://doi.org/10.1175/1520-0426(2002)019<0633:AMFETP>2.0.CO;2

Bringi, V. N., Williams, C. R., Thurai, M., & May, P. T. (2009). Using dual-polarized radar and dual-frequency profiler for DSD characterization: A case study from Darwin, Australia. *Journal of Atmospheric and Oceanic Technology*, *26*(10), 2107–2122. https://doi.org/10.1175/2009JTECHA1258.1

Burleyson, C. D., deSzoeke, S. P., Yuter, S. E., Wilbanks, M., & Brewer, W. A. (2013). Observations of the diurnal cycle of southeast Pacific marine stratocumulus clouds and precipitation. *Journal of the Atmospheric Sciences*, *70*(12), 3876–3894. https://doi.org/10.1175/JAS-D-13-01.1

Chang, A. T., Chiu, L. S., & Yang, G. (1995). Diurnal cycle of oceanic precipitation from SSM/I data. *Monthly Weather Review*, *123*(11), 3371–3380. https://doi.org/10.1175/1520-0493(1995)123<3371:DCOOPF>2.0.CO;2

Clothiaux, E. E., Ackerman, T. P., Mace, G. G., Moran, K. P., Marchand, R. T., Miller, M. A., & Martner, B. E. (2000). Objective determination of cloud heights and radar reflectivities using a combination of active remote sensors at the ARM CART sites. *Journal of Applied Meteorology and Climatology*, *39*(5), 645–665. https://doi.org/10.1175/1520-0450(2000)039<0645:ODOCHA>2.0.CO;2

Comstock, K., Wood, R., Yuter, S. E., & Bretherton, C. S. (2004). Reflectivity and rain rate in and below drizzling stratocumulus. *Quarterly Journal of the Royal Meteorological Society*, *130*(603), 2891–2918. https://doi.org/10.1256/qj.03.187

Dai, A., Lin, X., & Hsu, K.-L. (2007). The frequency, intensity, and diurnal cycle of precipitation in surface and satellite observations over low- and mid-latitudes. *Climate Dynamics*, *29*(7-8), 727–744. https://doi.org/10.1007/s00382-007-0260-y

Dolan, B., Fuchs, B., Rutledge, S. A., Barnes, E. A., & Thompson, E. J. (2018). Primary modes of global drop size distributions. *Journal of the Atmospheric Sciences*, *75*(5), 1453–1476. https://doi.org/10.1175/JAS-D-17-0242.1

Elsaesser, G. S., Kummerow, C. D., L'Ecuyer, T. S., Takayabu, Y. N., & Shige, S. (2010). Observed self-similarity of precipitation regimes over the tropical oceans. *Journal of Climate*, *23*(10), 2686–2698. https://doi.org/10.1175/2010JCLI3330.1

Elsaesser, G. S., O'Dell, C. W., Lebsock, M. D., Bennartz, R., Greenwald, T. J., & Wentz, F. J. (2017). The multisensor advanced climatology of liquid water path (MAC-LWP). *Journal of Climate*, *30*(24), 10,193–10,210. https://doi.org/10.1175/JCLI-D-16-0902.1

Feingold, G., Kreidenweis, S. M., Stevens, B., & Cotton, W. (1996). Numerical simulations of stratocumulus processing of cloud condensation nuclei through collision-coalescence. *Journal of Geophysical Research*, *101*(D16), 21,391–21,402. https://doi.org/10.1029/96JD01552

Fulton, R. A., Breidenbach, J. P., Seo, D., Miller, D. A., & O'Bannon, T. (1998). The WSR-88D rainfall algorithm. *Weather Forecasting*, *13*, 377–395. https://doi.org/10.1175/1520-0434(1998)013<0377:TWRA>2.0.CO;2

Gatlin, P. N., Thurai, M., Bringi, V. N., Petersen, W., Wolff, D., Tokay, A., et al. (2015). Searching for large raindrops: A global summary of two-dimensional video disdrometer observations. *Journal of Applied Meteorology and Climatology*, *54*(5), 1069–1089. https://doi.org/10.1175/JAMC-D-14-0089.1

Giangrande, S. E., Bartholomew, M. J., Pope, M., Collis, S., & Jensen, M. P. (2014). A summary of precipitation characteristics from the 2006–11 Northern Australian wet seasons as revealed by ARM disdrometer research facilities (Darwin, Australia). *Journal of Applied Meteorology and Climatology*, *53*(5), 1213–1231. https://doi.org/10.1175/JAMC-D-13-0222.1

Giangrande, S. E., Collis, S., Theisen, A. K., & Tokay, A. (2014). Precipitation estimation from the ARM distributed radar network during the MC3E campaign. *Journal of Applied Meteorology and Climatology*, *53*(9), 2130–2147. https://doi.org/10.1175/JAMC-D-13-0321.1

Giangrande, S. E., Toto, T., Bansemer, A., Kumjian, M. R., Mishra, S., & Ryzhkov, A. V. (2016). Insights into riming and aggregation processes as revealed by aircraft, radar, and disdrometer observations for a 27 April 2011 widespread precipitation event. *Journal of Geophysical Research: Atmospheres*, *121*, 5846–5863. https://doi.org/10.1002/2015JD024537

Hardin, J. (2014). PyDisdrometer Version v 1.0.

Hartmann, D. L., Ockert-Bell, M. E., & Michelsen, M. L. (1992). The effect of cloud type on Earth's energy balance: Global analysis. *Journal of Climate*, *5*(11), 1281–1304. https://doi.org/10.1175/1520-0442(1992)005%3C1281:TEOCTO%3E2.0.CO;2

Heistermann, M., Collis, S., Dixon, M. J., Giangrande, S., Helmus, J. J., Kelley, B., et al. (2015). The emergence of open-source software for the weather radar community. *Bulletin of the American Meteorological Society*, *96*(1), 117–128. https://doi.org/10.1175/BAMS-D-13-00240.1

Helmus, J. J., & Collis, S. M. (2016). The Python ARM Radar Toolkit (Py-ART), a library for working with weather radar data in the Python programming language. *Journal of Open Research Software*, *4*(1), e25. https://doi.org/10.5334/jors.119

Hou, A. Y., Kakar, R. K., Neeck, S., Azarbarzin, A. A., Kummerow, C. D., Kojima, M., et al. (2014). The global precipitation measurement (GPM) mission. *Bulletin of the American Meteorological Society*, *95*(5), 701–722. https://doi.org/10.1175/BAMS-D-13-00164.1

Houze, R. A. Jr. (2012). Orographic effects on precipitating clouds. *Reviews of Geophysics*, *50*, RG1001. https://doi.org/10.1029/2011RG000365

IPCC (2013). *Climate change 2013: The physical science basis: Contribution of Working Group I to the Fifth Assessment Report of the Intergovernmental Panel on Climate Change.* New York: Cambridge University Press.

Klein, S. A. (1997). Synoptic variability of low-cloud properties and meteorological parameters in the subtropical trade wind boundary layer. *Journal of Climate*, *10*(8), 2018–2039. https://doi.org/10.1175/1520-0442(1997)010<2018:SVOLCP>2.0.CO;2

Klein, S. A., & Hartmann, D. L. (1993). The seasonal cycle of low stratiform clouds. *Journal of Climate*, *6*(8), 1587–1606. https://doi.org/10.1175/1520-0442(1993)006<1587:TSCOLS>2.0.CO;2

Kollias, P., Jo, I., Borque, P., Tatarevic, A., Lamer, K., Bharadwaj, N., et al. (2014). Scanning ARM cloud radars. Part II: Data quality control and processing. *Journal of Atmospheric and Oceanic Technology*, *31*(3), 583–598. https://doi.org/10.1175/JTECH-D-13-00045.1

Kostinski, A. (2008). Drizzle rates versus cloud depths for marine stratocumuli. *Environmental Research Letters*, *3*(4), 45019. https://doi.org/10.1088/1748-9326/3/4/045019

Kruger, A., & Krajewski, W. F. (2002). Two-dimensional video disdrometer: A description. *Journal of Atmospheric and Oceanic Technology*, *19*(5), 602–617. https://doi.org/10.1175/1520-0426(2002)019<0602:TDVDAD>2.0.CO;2

Leinonen, J. (2014). High-level interface to T-matrix scattering calculations: Architecture, capabilities and limitations. *Optics Express*, *22*(2), 1655–1660. https://doi.org/10.1364/OE.22.001655

Leinonen, J., Moisseev, D., Leskinen, M., & Petersen, W. A. (2012). A climatology of disdrometer measurements of rainfall in Finland over five years with implications for global radar observations. *Journal of Applied Meteorology and Climatology*, *51*(2), 392–404. https://doi.org/10.1175/JAMC-D-11-056.1

Lhermitte, R. (2002). *Centimeter and millimeter wavelength radars in meteorology* (p. 550). Miami, FL: Lhermitte Publications.

Löffler-Mang, M., & Joss, J. (2000). An optical disdrometer for measuring size and velocity of hydrometeors. *Journal of Atmospheric and Oceanic Technology*, *17*, 130–139.

Mather, J. H., & Voyles, J. W. (2013). The ARM climate research facility: A review of structure and capabilities. *Bulletin of the American Meteorological Society*, *94*, 377–392.

Mechem, D. B., Wittman, C. S., Miller, M. A., Yuter, S. E., & de Szoeke, S. P. (2018). Joint synoptic and cloud variability over the Northeast Atlantic near the Azores. *Journal of Applied Meteorology and Climatology*, *57*(6). https://doi.org/10.1175/JAMC-D-17-0211.1

Miller, M. A., Jensen, M. P., & Clothiaux, E. E. (1998). Diurnal cloud and thermodynamic variations in the stratocumulus transition regime: A case study using in situ and remote sensors. *Journal of the Atmospheric Sciences*, *55*, 2294–2310.

Miller, M. A., Nitschke, K., Ackerman, T. P., Ferrell, W. R., Hickmon, N., & Ivey, M. (2016). Chapter 9: The ARM mobile facilities. *AMS Meteorological Monographs*, *57*, 9.1–9.15. https://doi.org/10.1175/AMSMONOGRAPHS-D-15-0051.1

Miller, M. A., & Yuter, S. E. (2013). Detection and characterization of heavy drizzle cells within subtropical marine stratocumulus using AMSR-E 89-GHz passive microwave measurements. *Atmospheric Measurement Techniques*, *6*, 1–13. https://doi.org/10.5194/amt-6-1-2013

Mishchenko, M. I. (2000). Calculation of the amplitude matrix for a nonspherical particle in a fixed orientation. *Applied Optics*, *39*, 1026–1031.

Naud, C. M., Booth, J. F., & Lamraoui, F. (2018). Post cold frontal clouds at the ARM Eastern North Atlantic site: An examination of the relationship between large-scale environment and low-level cloud properties. *Journal of Geophysical Research: Atmospheres*, *123*, 12,117–12,132. https://doi.org/10.1029/2018JD029015

Park, S.-G., Kim, H.-L., Ham, Y.-W., & Jung, S.-H. (2017). Comparative evaluation of the OTT PARSIVEL2 using a collocated two-dimensional video disdrometer. *Journal of Atmospheric and Oceanic Technology*, *34*, 2059–2082.

Pawlowska, H. (2003). An observational study of drizzle formation in stratocumulus clouds for general circulation model (GCM) parameterizations. *Journal of Geophysical Research*, *108*(D15), 8630. https://doi.org/10.1029/2002JD002679

Rapp, A., Lebsock, M., & L'Ecuyer, T. (2013). Low cloud precipitation climatology in the southeastern Pacific marine stratocumulus region using CloudSat. *Environmental Research Letters*, *8*(1), 014027. https://doi.org/10.1088/1748-9326/8/1/014027

Rapp, A. D. (2016). Observational evidence linking precipitation and mesoscale cloud fraction in the southeast Pacific. *Geophysical Research Letters*, *43*, 7267–7273. https://doi.org/10.1002/2016GL069906

Rémillard, J., Kollias, P., Luke, E., & Wood, R. (2012). Marine boundary layer cloud observations in the Azores. *Journal of Climate*, *25*(21), 7381–7398. https://doi.org/10.1175/JCLI-D-11-00610.1

Rémillard, J., & Tselioudis, G. (2015). Cloud regime variability over the Azores and its application to climate model evaluation. *Journal of Climate*, *28*(24), 9707–9720. https://doi.org/10.1175/JCLI-D-15-0066.1

Rogers, D. P., Yang, X., Norris, P. M., Johnson, D. W., Martin, G. M., Friehe, C. A., & Berger, B. W. (1995). Diurnal evolution of the cloud-topped marine boundary layer. Part I: Nocturnal stratocumulus development. *Journal of the Atmospheric Sciences*, *52*, 2953–2966.

Slingo, J. M. (1987). The development and verification of a cloud prediction scheme for the ECMWF model. *Quarterly Journal of the Royal Meteorological Society*, *113*, 899–927.

Snodgrass, E. R., Di Girolamo, L., & Rauber, R. M. (2009). Precipitation characteristics of trade wind clouds during RICO derived from radar, satellite, and aircraft measurements. *Journal of Applied Meteorology and Climatology*, *48*, 464–483.

Stephens, G. L., Vane, D. G., Boain, R. J., Mace, G. G., Sassen, K., Wang, Z., et al. (2002). The CloudSat mission and the A-train. *Bulletin of the American Meteorological Society*, *83*, 1771–1790. https://doi.org/10.1175/BAMS-83-12-1771

Stevens, B., Moeng, C.-H., Ackerman, A. S., Bretherton, C. S., Chlond, A., de Roode, S., et al. (2005). Evaluation of large-eddy simulations via observations of nocturnal marine stratocumulus. *Monthly Weather Review*, *133*, 1443–1462. https://doi.org/10.1175/MWR2930.1

Testud, J., Oury, S., Black, R. A., Amayenc, P., & Dou, X. (2001). The concept of "normalized" distribution to describe raindrop spectra: A tool for cloud physics and cloud remote sensing. *Journal of Applied Meteorology*, *40*, 1118–1140.

Thompson, E. J., Rutledge, S. A., Dolan, B., & Thurai, M. (2015). Drop size distributions and radar observations of convective and stratiform rain over the equatorial Indian and West Pacific Oceans. *Journal of the Atmospheric Sciences*, *72*, 4091–4125. https://doi.org/10.1175/JAS-D-14-0206.1

Thurai, M., Gatlin, P., Bringi, V. N., Petersen, W., Kennedy, P., Notaros, B., & Carey, L. (2017). Toward completing the raindrops size spectrum: Case studies involving 2D-video disdrometer, droplet spectrometer, and polarimetric radar measurements. *Journal of Applied Meteorology and Climatology*, *56*, 877–896.

Tokay, A., Petersen, W. A., Gatlin, P., & Wingo, M. (2013). Comparison of raindrop size distribution measurements by collocated disdrometers. *Journal of Atmospheric and Oceanic Technology*, *30*, 1672–1690. https://doi.org/10.1175/JTECH-D-12-00163.1

Tokay, A., Wolff, D. B., & Petersen, W. A. (2014). Evaluation of the new version of the laser-optical disdrometer, OTT Parsivel^2. *Journal of Atmospheric and Oceanic Technology*, *31*, 1276–1288. https://doi.org/10.1175/JTECH-D-13-00174.1

Tselioudis, G., Rossow, W., Zhang, Y.-C., & Konsta, D. (2013). Global weather states and their properties from passive and active satellite cloud retrievals. *Journal of Climate*, *26*, 7734–7746. https://doi.org/10.1175/JCLI-D-13-00024.1

vanZanten, M. C., Stevens, B., Vali, G., & Lenschow, D. H. (2005). Observations of drizzle in nocturnal marine stratocumulus. *Journal of the Atmospheric Sciences*, *62*(1), 88–106. https://doi.org/10.1175/JAS-3355.1

Wang, D., Giangrande, S. E., Bartholomew, M. J., Hardin, J., Feng, Z., Thalman, R., & Machado, L. A. T. (2018). The Green Ocean: precipitation insights from the GoAmazon2014/5 experiment. *Atmospheric Chemistry and Physics*, *18*, 9121–9145. https://doi.org/10.5194/acp-18-9121-2018

Wood, R. (2005). Drizzle in stratiform boundary layer clouds. Part I: Vertical and horizontal structure. *Journal of the Atmospheric Sciences*, *62*(9), 3011–3033. https://doi.org/10.1175/JAS3529.1

Wood, R., O, K., Bretherton, C. S., Mohrmann, J., Albrecht, B. A., Zuidema, P., et al. (2018). Ultraclean layers and optically thin clouds in the stratocumulus-to-cumulus transition. Part I: Observations. *Journal of the Atmospheric Sciences*, *75*, 1631–1652. https://doi.org/10.1175/JAS-D-17-0213.1

Wood, R., Wyant, M., Bretherton, C. S., Rémillard, J., Kollias, P., Fletcher, J., et al. (2015). Clouds, aerosols, and precipitation in the marine boundary layer: An ARM mobile facility deployment. *Bulletin of the American Meteorological Society*, *96*(3), 419–440. https://doi.org/10.1175/BAMS-D-13-00180.1

Yang, F., Luke, E. P., Kollias, P., Kostinski, A. B., & Vogelmann, A. M. (2018). Scaling of drizzle virga depth with cloud thickness for marine stratocumulus clouds. *Geophysical Research Letters*, *45*, 3746–3753. https://doi.org/10.1029/2018GL077145

Zhou, X., Heus, T., & Kollias, P. (2017). Influences of drizzle on stratocumulus cloudiness and organization. *Journal of Geophysical Research: Atmospheres*, *122*, 6989–7003. https://doi.org/10.1002/2017JD026641